Institution of
**MECHANICAL
ENGINEERS**

Journal of
SYSTEMS AND CONTROL
ENGINEERING

Adaptive backstepping human-cooperative control of a pediatric gait exoskeleton system with high- and low-level admittance

Jyotindra Narayan[1] [iD]**, Bhaben Kalita[2]**[iD] **and Santosha K Dwivedy[1]**

Abstract

Post-neurological disorder, passive-assist training disregards human involvement during robot-aided lower-limb rehabilitation. This work presents a novel human-cooperative framework based on the admittance and trajectory control scheme to administer the subject–exoskeleton interaction for pediatric gait rehabilitation. Initially, the mechanical design and dynamic analysis of an existing exoskeleton system are briefly attended. Thereafter, an admittance model is designed in the outer loop, which recasts the desired human trajectory into a reference trajectory. As an inner-loop control scheme, a robust adaptive backstepping controller is designed to trace the reference gait trajectory under parametric uncertainties and external disturbances. Lyapunov stability analysis is solved to guarantee the uniform boundedness of the control signals. Moreover, the well-known problem of "explosion of complexity" and "overparameterization" is avoided through the design of the robust adaptive backstepping control scheme. The performance of the proposed robust adaptive backstepping-based human-cooperative control is studied under the low- and high-level admittance model. Finally, the effectiveness of the proposed control is validated with a variable structure adaptive robust-based human-cooperative control. The co-simulation results show that the proposed control with low-level admittance allows the subject to participate in the training process more frankly. The proposed robust adaptive backstepping-based human-cooperative control tracks the reference gait more promisingly than the variable structure adaptive robust-based human-cooperative control for both admittance levels.

Keywords

Human cooperative, subject–exoskeleton interaction, adaptive backstepping, admittance

Introduction

A significant rise in neurological diseases (stroke, spinal cord injury (SCI), and cerebral palsy (CP)) is observed for different age ranges with the increase in the global population. The Global Burden of Disease (GBD) reported in 2019 that "stroke" is the second primary reason of disability for the elderly population.[1] However, the stroke incidence for the pediatric age group is recorded as 2.5–13 per 100,000/year.[2] The prevalence of CP is observed as 2.95 per 1000 sample size in the developing countries.[3] Among people suffering from neurological diseases, dyskinesia is a common problem resulting in partial or complete paralytic conditions in their lower limits. Several studies emphasize the importance of appropriate and repetitive rehabilitation training by physical therapists to improve motor

function in the lower limbs.[4,5] However, traditional rehabilitation techniques can be cumbersome, causing fatigue for therapists and relying on skilled staff with limited sustainability. To address these challenges, designers and researchers have developed various single- and multi-joint lower-limb exoskeleton robots (LLERs), as extensively reviewed by Kalita et al.[6]

[1]Department of Mechanical Engineering, Indian Institute of Technology Guwahati, Guwahati, India
[2]Terrestrial Robotics Engineering & Controls (TREC) Laboratory, Virginia Tech, Blacksburg, VA, USA

Corresponding author:
Jyotindra Narayan, Department of Mechanical Engineering, Indian Institute of Technology Guwahati, Guwahati 781039, Assam, India.
Email: n.jyotindra@gmail.com

Rehabilitation training using exoskeleton robots can be broadly categorized into two modes based on the subject's participation: passive-assist (PA) mode and active-assist (AA) mode.[7,8] In PA mode, the subject's limbs are majorly regulated by the exoskeleton with minimal interaction between the subject and the human, which helps to lessen muscular atrophy problems. Furthermore, when the patient recovers and regains significant muscle energy in their lower limbs, their active participation becomes advantageous for achieving effective training outcomes. This cooperation between the subject and the exoskeleton leads to the AA mode, where the subject uses their muscle energy in conjunction with the assistance provided by the exoskeleton. It is important to note that the collaboration between humans and robots in this mode can potentially cause joint misalignment and generate interaction forces. These interaction forces can be measured in different ways, that is, using force/torque sensors,[9,10] spring-damper models,[11,12] and disturbance observers.[13,14] The selection of appropriate control schemes plays a crucial role in implementing gait exoskeleton robots in various therapy settings. The PA mode primarily uses position/trajectory control as the prevailing control scheme. In contrast, the AA mode commonly incorporates both position/trajectory control and impedance/admittance control.

In the past two decades, extensive research has been conducted on position/trajectory control methods for LLERs, including both non-robust[15,16] and robust approaches[17–22] for the LLERs to achieve a predefined gait trajectory. However, the position control schemes could never be sufficient in physical human–robot interaction (pHRI) where the subject's active involvement is crucial in lower-limb rehabilitation. As a result, researchers have been investigating the integration of impedance/admittance control with position/trajectory control in the last few years to enhance the active engagement of the user. Vallery et al.[23] proposed an approach of generalized elasticities to mitigate the effects of the interaction forces. However, in the context of AA training, instead of attempting to mitigate the effects of interaction forces, these forces should be taken into consideration to regulate the level of assistance provided to the user. Saglia et al.[24] introduced admittance control in a rehabilitation robot to treat musculoskeletal ankle injuries. Ayas and Altas[25] presented fuzzy logic admittance control for two degrees of freedom (2-DOFs) ankle rehabilitation robot on adapting different assistance/resistance levels of patients. Both previous studies have only focused on ankle rehabilitation and considered non-robust position control schemes for tracking the gait trajectory in real time. Luo et al.[26] exploited the Central Pattern Generator (CPG) with fuzzy logic to adjust the impedance parameters per the subject's involvement. However, the actual design of the exoskeleton robot and position controller is unclear in their study. Furthermore, electromyography (EMG) and

electroencephalogram (EEG) signals are extensively used in AA lower-limb rehabilitation, where EMG-based control[10] calls for significant muscle activation and EEG-based control[27] necessitates a high concentration of patients. As observed from the above studies, most human-cooperative control designs have used the non-robust trajectory control in the inner loop to track the altered gait. However, this approach may not be adequate in situations involving parametric variations and external disturbances, such as unpredictable movements or involuntary muscle contractions.

Referring above challenges and to deal with such uncertain variations and external disturbances, sliding surface-based trajectory tracking control strategies have been incorporated to follow the modified reference gait in case of human–robot interaction.[9,28–32] Torabi et al.[28] proposed a cooperative control based on an adaptive sliding mode control (SMC) in the inner loop and admittance control in the outer loop for a two-link coupled lower limb of the subject and exoskeleton. However, they have considered the admittance model with fixed values instead of varying ones. In another work, Almaghout et al.[29] exploited a super-twisting non-singular terminal SMC to perform therapeutic training with finite-time convergence of the error states. However, the effect of selecting different admittance levels was not explored. In other work on robust inner-loop position control, Mokhtari et al.[30] designed an adaptive high-order super-twisting SMC for an LLER to attenuate chattering. Although the authors obtained the optimal impedance parameters, they have not considered the varying impedance model as in the case of the real environment during AA gait rehabilitation. In work on coordinated movement, Zhang et al.[31] presented a sliding mode adaptive-based assist-as-needed control scheme for a lower-limb exoskeleton system. However, instead of explicitly focusing on impedance/admittance control, they have considered the radial basis function (RBF) neural networks with a forgetting factor to regulate the torque assistance. Shen et al.[32] proposed a variable structure adaptive robust-based human-cooperative control (VSAR-HCC) for a three-DOFs lower-limb exoskeleton system that exploits a sliding surface-based adaptive control in an outer loop and follows an admittance control in the outer loop with a variable gain. In other work by Tu et al.,[9] an intent-based variable admittance model along with the robust adaptive SMC was proposed for an active hip-knee exoskeleton system, where model uncertainty was estimated using RBF neural network. Except for the work by Torabi et al.,[28] the aforementioned studies have employed the approach of lumped parameter estimation. However, a limitation of this approach is its reliance on the approximate evaluation of uncertainties rather than achieving a precise estimation of various model parameters.

For precise estimation of model parameters, backstepping control (BC) has been used with the

appropriate adaptation laws, termed adaptive back-stepping control (ABC), to deal with uncertainties and disturbances of dynamical system.[33,34] The design of ABC is a stepwise recursive method that inherently suffices the stability criteria using proper Lyapunov functions. However, such control designs sometimes have shortcomings, such as overparameterization, high-control signals, and the explosion of terms. The problem of overparametrization could be addressed by pushing the parameter estimation to the final step and formulating the estimation function based on the error between actual states and virtual variables.[35] Guo et al.[36] proposed neural network-based ABC to mitigate the large magnitudes of control signals. The first-order filter[37,38] and second-order command filter with SMC scheme[39] have been employed to deal with the explosion of terms in conventional BC. However, it is worth noting that the design process of ABC with filters becomes computationally expensive.

This study introduces a filter-free adaptive backstepping human-cooperative control with adjustable admittance levels to offer several benefits within the human–robot interaction framework, such as the variable assistance level in AA mode, robust position control for effective gait tracking, and the precise estimation of model parameters for a coupled human–exoskeleton system. To the authors' best knowledge, there is hardly any study available on the design of a robust adaptive backstepping human-cooperative control (RAB-HCC) for a pediatric exoskeleton system. Inspired by the work of Zhang et al.,[35] the present work addresses the over-parameterization problem by keeping the first design step free from any unknown parameters estimation and postponing the estimation process generically to the last design step. The proposed design in this work avoids the "explosion of complexity" by selecting an appropriate virtual control law that avoids the inertial, centrifugal, and gravity matrices during differentiation. Based on the preceding statements, the notable contributions of this study can be outlined as follows:

1. To design and investigate the effects of a low- and high-level admittance model for a pediatric lower-limb exoskeleton in AA training mode as compared to fixed admittance model in the work by Torabi et al.[28]
2. To propose an RAB-based reference trajectory controller with avoidance of "overparameterization" and "explosion of terms" using a systematic construct of Lyapunov candidate function and an appropriate virtual control law. Unlike existing works,[37–39] the proposed RAB control involves a filter-free approach that reduces the computational complexity of the human-cooperative framework.
3. To propose a regressor matrix-based adaptive law in the BC to precisely estimate the parametric uncertainties as compared to the lumped parameter approximation approach given in existing works.[9,32]

4. To investigate the potential of proposed RAB-HCC by comparing it with a contrast cooperative control named VSAR-HCC given in Shen et al.[32]

Coupled human–exoskeleton overview

The mechanical strength and stability of the LLER in standstill and working positions are essential to design. The robot's power is characterized by the load-bearing capability of joints, chassis frame, and other connecting components. The exoskeleton structure should sustain different static and varying loads during motion assistance and gait rehabilitation, especially in AA mode. Although the device is tailored as patient-specific, it should be able to accommodate different sizes of the patient, which may change in due course of training time. In addition, an exoskeleton should be initially designed and developed with the necessary DOF instead of providing all possible DOFs to maintain the safety standards of the user.

Mechanical design

With the consideration of different design factors, Narayan and Dwivedy[40] introduced an initial setup of a six DOFs exoskeleton robot (LLES *v*1) for pediatric gait rehabilitation where a wheeler stand was appended at the back to warrant safety for both the user and the robot. Furthermore, the design of LLES *v*1 was modified to LLES *v*2 for better rigidity of stand support, decreased link masses, the simplified arrangement of the hip motors, variable waist size, and free movements of the stand wheels.[41] The current version, (LLES *v*2) as shown in Figure 1, is dedicated to serving children aged 8–12 years, with a body mass of 25–40 kg and a constant body height of 130 ± 2 cm. There are three active joints in the sagittal plane with LLES *v*2 for moving the human's lower limbs, that is, hip flexion/extension (f/e), knee flexion/extension (f/e), and ankle dorsi/plantar flexion (d/p). The ankle joint is designed with the assumption that the ground reaction forces (GRF) are generated by the user's foot reaction irrespective of the training mode. Figure 1(a)–(c) illustrate the computer-aided design (CAD) and Figure 1(d) shows the functional prototype of the LLES *v*2 with subject.

Both the hip joints of the exoskeleton are actuated with the help of two heavy-duty planetary-geared DC motors mounted over the wheeler stand. A pair of linear lead-screw actuators are attached to each leg's thigh and shank link to drive the knee joints. A low-capacity DC motor is employed to move the ankle joint in the swing and stance phase, and the subject can mimic the gait cycle more effectively using the active ankle joint. The selection of the ratings of the used actuators in the overall design and prototype of LLES is decided based on the control studies carried out by the authors for PA training mode.[19,42] To ensure the safety of the subject, the maximum possible ranges of motion (ROM) for different lower-limb joints are in line with the work by
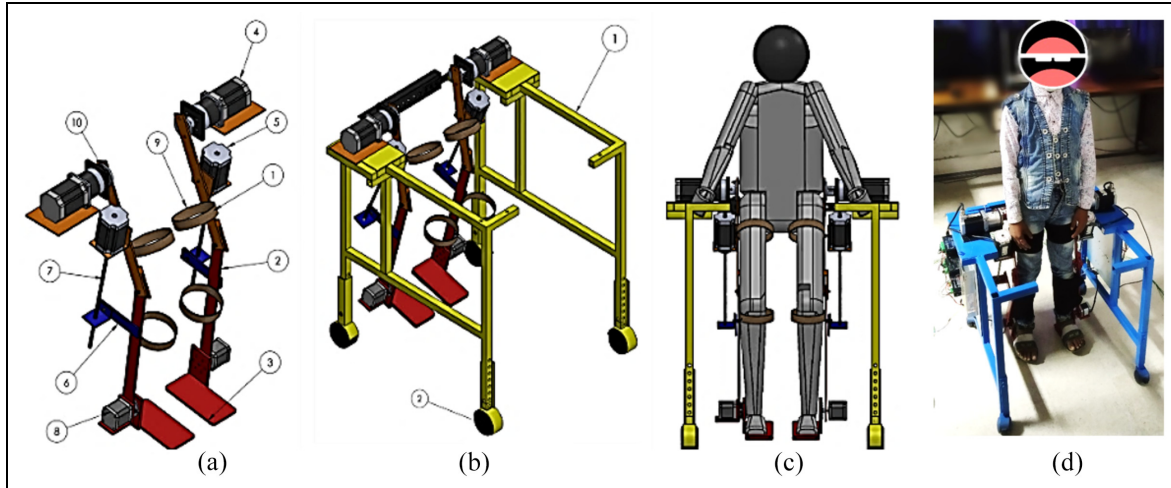
Figure 1. CAD model. (a) LLES v2 (Labels: 1. Thigh link, 2. Shank link, 3. Foot link, 4. Hybrid stepper motor, 5. Lead screw actuator, 6. Extended shank link, 7. Lead screw, 8. Stepper motor, 9. Holding splints, 10. Coupler). (b) Exoskeleton assembly (Labels: 1. Stand assembly, 2. Wheel support). (c) Exoskeleton with a human dummy. (d) Developed prototype of LLES v2.
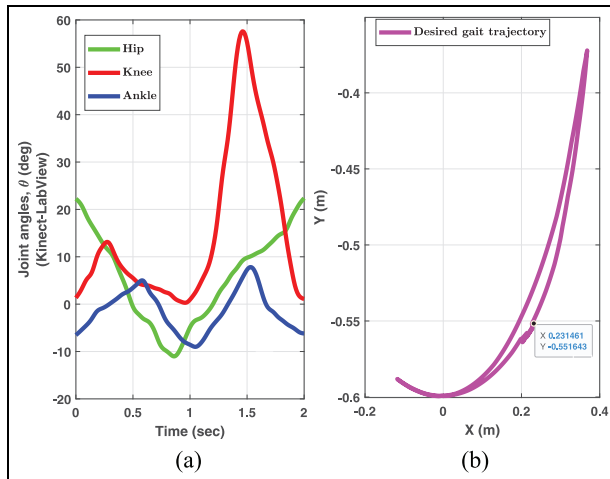

Figure 2. Experimental gait data. (a) Desired joint angular trajectory. (b) Desired gait trajectory.

Table 1. Specifications of LLES v2 and human child.

	Part	Mass (kg)	Length (m)
LLES	Thigh link	$m_1^e = 4.55$	$l_1^e = 0.30$
	Shank link	$m_2^e = 1.70$	$l_2^e = 0.28$
	Foot link	$m_3^e = 0.75$	$l_3^e = 0.08$
Child (8 years of age)	Thigh	$m_1^h = 4.25$	$l_1^h = 0.28$
	Shank	$m_2^h = 2.75$	$l_2^h = 0.26$
	Foot	$m_3^h = 0.80$	$l_3^h = 0.04$

estimate the joint angles in the sagittal plane. The desired gait trajectory in joint space and Cartesian space (X, Y) is illustrated in Figure 2(a) and (b), respectively. The ROM for hip, knee, and ankle joints is recorded as 22.3° to −9.35°, 58.34° to 1.12°, and 5.3° to −8.11° for an 8-year-old child, respectively.

Chester et al. and Cigali et al.[43,44] and as follows: 30°/−12° for the hip (f/e), 60°/−10° for the knee (f/e), and 13°/−20° for the ankle (d/p). Moreover, an emergency stop button is integrated into the software and hardware interface. The stop button can be used in the software as the joint moves beyond the allowable ROM. The subject can activate the switch to terminate the complete training process in case of discomfort during a rehabilitation session.

The decomposition of lower-limb parameters for the pediatric subject and exoskeleton is given in Table 1. The joint and Cartesian space reference trajectory is computed for an 8-year-old male child (body mass: 34 kg, body height: 127 cm) using a Kinect-LabVIEW-based motion capture (MOCAP) system. The interested reader may follow the authors' previous work[45] on the generalized setting of such MOCAP systems to

Dynamic modeling

In general, two major characteristics of the exoskeleton robot are the synchronization of joint movements and physical interaction with the human. In dynamic modeling of the LLERs, researchers have usually addressed the problem of syncing the robot's joint movements with the human and ignored the aspects of pHRI. In this work, the dynamic model of the coupled subject–exoskeleton is considered with the effects of pHRI. Assuming a three-link structure aligned with the lower-extremity segments (Figure 3), the Euler–Lagrange principle is used to model the generalized state-space dynamics of a coupled system as below

$$\tau^h = \mathcal{M}^h(q^h)(\ddot{q}^h) + \mathcal{C}^h(q^h, \dot{q}^h)\dot{q}^h + \mathcal{G}^h(q^h) \tag{1}$$

$$\tau^e = \mathcal{M}^e(q^e)\ddot{q}^e + \mathcal{C}^e(q^e, \dot{q}^e)\dot{q}^e + \mathcal{G}^e(q^e) \tag{2}$$
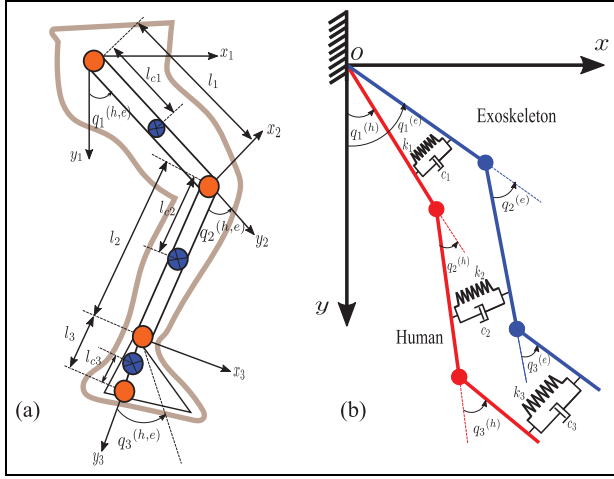
Figure 3. Coupled human–exoskeleton model. (a) A simplified linkage structure ($l_1 : l_1^e, l_1^h; l_2 : l_2^e, l_2^h; l_3 : l_3^e, l_3^h$) denote the thigh, calf, and foot length of the exoskeleton and human. l_{c1}, l_{c2}, and l_{c3} signify the center of mass distance for the respective lengths). (b) Interaction dynamics ($c : c_1, c_2, c_3$ and $k : k_1, k_2, k_3$ represent the damping and spring coefficient of the thigh, calf, and foot bracing straps.

Here, $\tau^h = [\tau_1^h, \tau_2^h, \tau_3^h]^T$ and $\tau^e = [\tau_1^e, \tau_2^e, \tau_3^e]^T$ denote joint torque vectors for human subject and exoskeleton system, respectively; $q^h = [q_1^h, q_2^h, q_3^h]^T$ and $q^e = [q_1^e, q_2^e, q_3^e]^T$ are state vectors of human and exoskeleton joint angle, respectively; $\dot{q}^h = [\dot{q}_1^h, \dot{q}_2^h, \dot{q}_3^h]^T$ and $\dot{q}^e = [\dot{q}_1^e, \dot{q}_2^e, \dot{q}_3^e]^T$ are joint speed vectors of human and exoskeleton, respectively; $\ddot{q}^h = [\ddot{q}_1^h, \ddot{q}_2^h, \ddot{q}_3^h]^T$ and $\ddot{q}^e = [\ddot{q}_1^e, \ddot{q}_2^e, \ddot{q}_3^e]^T$ are joint acceleration vectors of human and exoskeleton, respectively; $\mathcal{M}^h(q^h) \in \mathbb{R}^{3 \times 3}$ and $\mathcal{M}^e(q^e) \in \mathbb{R}^{3 \times 3}$ are the positive-definite inertial matrices of human and exoskeleton, respectively; $\mathcal{C}^h(q^h, \dot{q}^h) \in \mathbb{R}^{3 \times 3}$ and $\mathcal{C}^e(q^e, \dot{q}^e) \in \mathbb{R}^{3 \times 3}$ hold Coriolis/centrifugal effects of human and exoskeleton in matrix form, respectively; and $\mathcal{G}^h(q^h) \in \mathbb{R}^3$ and $\mathcal{G}^e(q^e) \in \mathbb{R}^3$ refer the gravitational vectors for human and exoskeleton, respectively. The element-wise expression of inertia, Coriolis/centrifugal, and gravity matrix is presented in Appendix 1 from authors' previous works.[20,40]

Furthermore, the flexible coupling braces bring about the interaction forces between the lower extremity of the human and the respective exoskeleton link. The generated reaction torque behaves as an appurtenance to the subjects with partial muscle strength while acting as a recalcitrant for the exoskeleton system. A schematic representation of the human–exoskeleton interaction is shown in Figure 3(a) and (b). Consequently, the dynamics of the coupled system can be interpreted as follows

$$\tau^h + \tau^{int} = \mathcal{M}^h(q^h)(\ddot{q}^h) + \mathcal{C}^h(q^h, \dot{q}^h)\dot{q}^h + \mathcal{G}^h(q^h) \quad (3)$$

$$\tau^e - \tau^{int} = \mathcal{M}^e(q^e)\ddot{q}^e + \mathcal{C}^e(q^e, \dot{q}^e)\dot{q}^e + \mathcal{G}^e(q^e) \quad (4)$$

where $\tau^{int} = [\tau_1^{int}, \tau_2^{int}, \tau_3^{int}]^T$ refers to the interaction torque.

In PA mode, the subject's limbs are entirely supervised by the exoskeleton, with the least possible interaction between the subject and the human. In that case, the subject's limb segments closely align with the exoskeleton's segments. Therefore, connections are assumed to be rigid even with viscoelastic bracing straps. However, in AA mode, while the limb is still strapped with the exoskeleton using viscoelastic braces, the subject exerts their muscle energy in conjugation with the exoskeleton power that leads to the joint's misalignment. Such non-compliant movements between the exoskeleton and subject induce interaction forces, and connections are assumed to be flexible. In real-time experiments, expensive sensor devices estimate the interaction forces/torques directly. Due to the extensive studies available on spring-damper-based mathematical model,[11,12] one can replicate the behavior of the coupling material and avoid the cost of expensive force sensors. Following Figure 3(b), the interaction torque can be modeled as below

$$\tau^{int} = J^T f^{int} = J^T \left(c\left(\dot{x}_i^e - \dot{x}_i^h\right) + k\left(x_i^e - x_i^h\right) \right) = c\left(\dot{q}^e - \dot{q}^h\right) + k\left(q^e - q^h\right) \quad (5)$$

Here, f^{int} signifies interaction forces; J^T is the transpose of Jacobian matrix depending on the bracing locations; $(\dot{x}_i^e - \dot{x}_i^h)$ and $(x_i^e - x_i^h)$ represent the velocity and position disparity at the bracing locations, respectively; $(\dot{q}^e - \dot{q}^h)$ and $(q^e - q^h)$ signifies the difference in angular velocity and angular position; c and k are the damping and spring constant factors of the braces (strap material) in Ns/m and N/m, respectively.

Furthermore, considering the frictional interference and external disturbances in the dynamic model, the relation of the exoskeleton robot in equation (6) can be represented as follows

$$\tau^e - \tau^{int} + \tau_d = \mathcal{M}^e(q^e)\ddot{q}^e + \mathcal{C}^e(q^e, \dot{q}^e)\dot{q}^e + \mathcal{G}^e(q^e) + \mathcal{F}(\dot{q}^e) \quad (6)$$

Here, $\tau_d \in \mathbb{R}^3$ is the disturbance vector and $\mathcal{F}(\dot{q}^e) \in \mathbb{R}^3$ denotes the friction model comprising the Coulomb friction $C_f \in \mathbb{R}^3$ and viscous friction $\mathcal{V}_f \in \mathbb{R}^3$. The friction model is formulated as

$$\mathcal{F}(\dot{q}^e) = C_f \mathrm{sgn}(\dot{q}^e) + \mathcal{V}_f = C_f \mathrm{sgn}(\dot{q}^e) + \sigma \dot{q}^e \quad (7)$$

where σ denotes the velocity factor in Nm/rad^{-1}, and *sgn* represents the signum function. The dynamic model, presented in equation (6), holds the following two properties (P1 and P2) and an assumption (A).[46]

(P1) $\mathcal{M}^e(q^e)$ poses symmetric and positive-definite behavior in the matrix form and holds the following relation

$$\tilde{a}_1 \parallel \beta \parallel^2 \leqslant \beta^T \mathcal{M}^e(q^e)\beta \leqslant \tilde{a}_2 \parallel \beta \parallel^2 \ \ \forall \beta \in \mathbb{R}^3 \quad (8)$$

where $\tilde{a}_1$ and $\tilde{a}_2$ are positive constants.

(P2) $\dot{\mathcal{M}}^e(q^e) - 2\mathcal{C}^e(q^e, \dot{q}^e)$ holds a behavior of skew-symmetric matrix when $\forall f \in \mathbb{R}^3$

$$f^T(\dot{\mathcal{M}}^e(q^e) - 2\mathcal{C}^e(q^e, \dot{q}^e))\varrho = 0 \quad (9)$$

(A)   The external disturbances are bounded in such a way as to confirm the following condition

$$||\tau_d|| \leqslant \bar{\tau}_d \quad (10)$$

where $\bar{\tau}_d$ denotes a positive constant.

Human-cooperative controller design

The human-cooperative control involves a hierarchy-type control framework to allow the subject's active participation, as discussed in the "Introduction" section. In this work, the outer-loop control is considered as admittance control, while the inner-loop control is presented as a robust adaptive backstepping position control. The following subsections present the design of admittance control first and then the position control vis-a-vis coupled pediatric-exoskeleton system.

Outer-loop control: admittance control

The admittance control allows the exoskeleton robot to alter its desired trajectory based on the interaction force applied by the subject. The modified trajectory complies with the subject–exoskeleton interaction force, which depends on the deviation between the original human trajectory and the actual exoskeleton trajectory. The tracking of modified reference trajectory by the exoskeleton is dealt with using a low-level controller. If the desired (original human) gait trajectory is q^h and the reference (modified) gait trajectory is q^r, then the admittance model can be designed as

$$M_a(\ddot{q}^h - \ddot{q}^r) + C_a(\dot{q}^h - \dot{q}^r) + K_a(q^h - q^r) = \tau^{int}$$
$$(11)$$

$$\ddot{q}^r = \ddot{q}^h - M_a^{-1}\{C_a(\dot{q}^h - \dot{q}^r) + K_a(q^h - q^r) - \tau^{int}\} \quad (12)$$

where M_a, C_a, K_a denote the inertia, damping, and stiffness admittance parameters. It is evident from equations (11) and (12) that if interaction torque is negligible, then $q^r = q^h$ which represents the case of PA training mode.

Inner-loop control: robust adaptive backstepping trajectory control

The concept of adaptive backstepping[47,48] is used to design the robust structure of trajectory tracking control for the lower-limb exoskeleton system during AA rehabilitation. The proposed design is focused on controlling the reference gait with parametric uncertainties and external perturbations. The Lyapunov candidate function is implicitly exploited to confirm the uniform boundedness of the closed-loop signals. The coupled human–exoskeleton model in parametric strict-feedback form can be indicated as follows

$$s_1 = q^e, \ s_2 = \dot{q}^e, \ s = [s_1, s_2]^T \quad (13)$$

$$\begin{cases} \dot{s}_1 = s_2 \\ \dot{s}_2 = \mathcal{M}^{e^{-1}}(q^e)(\tau^e - \tau^{int} + \tau_d - \mathcal{C}^e(q^e, \dot{q}^e)\dot{q}^e \\ \quad\quad - \mathcal{G}^e(q^e) - \mathcal{F}(\dot{q}^e)) \end{cases} \quad (14)$$

Here, $s_1 \in \mathbb{R}^3$, $s_2 \in \mathbb{R}^3$ are the state vectors of the exoskeleton robot. The gait tracking error variables can be selected as

$$\xi_1 = q^e - q^r \quad (15)$$

$$\xi_2 = \dot{\xi}_1 - \zeta = s_2 - \dot{q}^r - \zeta \quad (16)$$

where ζ represents the virtual controller for stabilizing the dynamical system.

The primary purpose is to ensure the tracking of the reference trajectory q^r by the actual trajectory q^e under dynamic uncertainties. Hence, a stepwise process can be employed to design trajectory tracking control which is given below.

Step 1. The second error variable ξ_2 and virtual control parameter ζ can be exploited to define the derivative of the first error variable ξ_1 as follows

$$\dot{\xi}_1 = \dot{s}_1 - \dot{q}^r = s_2 - \dot{q}^r = \xi_2 + \zeta \quad (17)$$

At first, the Lyapunov function can be specified as below

$$\mathcal{L}_1 = \frac{1}{2}\left(\xi_1{}^T\xi_2\right) \quad (18)$$

Incorporating equation (17) in the derivative of equation (18), the following relation can be obtained

$$\dot{\mathcal{L}}_1 = \xi_1^T \dot{\xi}_1 = \xi_1^T \xi_2 + \xi_1^T \zeta \qquad (19)$$

The virtual control law ζ can be expressed as

$$\zeta = -\epsilon_1 \xi_1 = -\epsilon_1 s_1 + \epsilon_1 q^r \qquad (20)$$

where ϵ_1 is a diagonal positive matrix. Now, using equations (19) and (20), equation (19) can be rewritten as follows

$$\dot{\mathcal{L}}_1 = -\xi_1^T \epsilon_1 \xi_1 + \xi_1^T \xi_2 \qquad (21)$$

It is worth noting from the above relation that $\dot{\mathcal{L}}_1$ is negative definite for $\xi_2 = 0$, which ensures the convergence of the first error variable ξ_1.

Step 2. The derivative of the second error variable $\dot{\xi}_2$ can be formulated as follows

$$\begin{aligned}
\dot{\xi}_2 = \dot{s}_2 - \dot{\zeta} - \ddot{q}^r &= \mathcal{M}^{e^{-1}}(q^e)(\tau^e - \tau^{int} + \tau_d \\
&- \mathcal{C}^e(q^e, \dot{q}^e)\dot{q}^e - \mathcal{G}^e(q^e) - \mathcal{F}(\dot{q}^e)) \\
&- \dot{\zeta} - \ddot{q}^r
\end{aligned} \qquad (22)$$

where

$$\dot{\zeta} = -\epsilon_1 \dot{s}_1 + \epsilon_1 \dot{q}^r = -\epsilon_1 s_2 + \epsilon_1 \dot{q}^r \qquad (23)$$

Now, an appropriate Lyapunov function depending on the property (P1) (equation (8)), can be chosen as follows

$$\bar{\mathcal{L}}_2 = \mathcal{L}_1 + \mathcal{L}_2 = \mathcal{L}_1 + \frac{1}{2}\left(\xi_2^T \mathcal{M}^e(q^e)\xi_2\right) \qquad (24)$$

The derivative of the Lyapunov function in equation (24) can be formulated as

$$\dot{\bar{\mathcal{L}}}_2 = \dot{\mathcal{L}}_1 + \xi_2^T \mathcal{M}^e(q^e)\dot{\xi}_2 + \frac{1}{2}\xi_2^T \dot{\mathcal{M}}^e(q^e)\xi_2 \qquad (25)$$

Furthermore, exploiting the property (P2) (equation (9)), the above relation can be modified as follows

$$\dot{\bar{\mathcal{L}}}_2 = \dot{\mathcal{L}}_1 + \xi_2^T\left(\mathcal{M}^e(q^e)\dot{\xi}_2 + \mathcal{C}^e(q^e, \dot{q}^e)\xi_2\right) \qquad (26)$$

Based on equations (16) and (22), the expression $\mathcal{M}^e(q^e)\dot{\xi}_2 + \mathcal{C}^e(q^e, \dot{q}^e)\xi_2$ in equation (26) can be expressed as

$$\begin{aligned}
\mathcal{M}^e(q^e)\dot{\xi}_2 + \mathcal{C}^e(q^e, \dot{q}^e)\xi_2 &= \mathcal{M}^e(q^e)\left(\dot{s}_2 - \dot{\zeta} - \ddot{q}^r\right) \\
&+ \mathcal{C}^e(q^e, \dot{q}^e)(s_2 - \zeta - \dot{q}^r) = \mathcal{M}^e(q^e)\left(-\dot{\zeta} - \ddot{q}^r\right) \\
&+ \mathcal{C}^e(q^e, \dot{q}^e)(-\zeta - \dot{q}^r) + \tau^e - \tau^{int} + \tau_d - \mathcal{G}^e(q^e) - \mathcal{F}(\dot{q}^e)
\end{aligned} \qquad (27)$$

However, the dynamic parameters in the coupled human–exoskeleton system are not truly known in real scenarios, thereby invoking the matrices of equation (27) in the design of the trajectory tracking control scheme is inaccurate. To overcome such problems, an adaptation law is considered to estimate the dynamic uncertainties. The right-hand side of equation (27), representing the unknown model parameters, can be rearranged as

$$\begin{aligned}
\mathcal{M}^e(q^e)\left(-\dot{\zeta} - \ddot{q}^r\right) &+ \mathcal{C}^e(q^e, \dot{q}^e)(-\zeta - \dot{q}^r) + \tau^e - \tau^{int} \\
&+ \tau_d - \mathcal{G}^e(q^e) - \mathcal{F}(\dot{q}^e) = \Phi\Omega + \tau^e - \tau^{int} + \tau_d - \mathcal{F}(\dot{q}^e)
\end{aligned} \qquad (28)$$

Thereafter, equation (26) can be represented as follows

$$\dot{\bar{\mathcal{L}}}_2 = \dot{\mathcal{L}}_1 + \xi_2^T\left(\Phi\Omega + \tau^e - \tau^{int} + \tau_d - \mathcal{F}(\dot{q}^e)\right) \qquad (29)$$

where $\Phi \in \mathbb{R}^{3 \times 16}$ signifies a regression matrix derived from the sensor-based feedback and $\Omega \in \mathbb{R}^{16 \times 1}$ refers to the set of unknown parameters (refer Appendix 2). As per the earlier discussion, the Lyapunov function from equation (24) can be modified as given below

$$\mathcal{L} = \bar{\mathcal{L}}_2 + \frac{1}{2}\tilde{\Omega}\Pi^{-1}\tilde{\Omega}; \quad \tilde{\Omega} = \Omega - \hat{\Omega} \qquad (30)$$

Here, $\tilde{\Omega}$ indicates the estimation of the unknown parameters in matrix form, and Π denotes an arbitrarily selected positive-definite matrix. Now, the following expression can be obtained after differentiating equation (30)

$$\begin{aligned}
\dot{\mathcal{L}} = \dot{\bar{\mathcal{L}}}_2 - \tilde{\Omega}^T\Pi^{-1}\dot{\hat{\Omega}} &= \dot{\mathcal{L}}_1 - \tilde{\Omega}^T\Pi^{-1}\dot{\hat{\Omega}} + \\
&\xi_2^T\left(\Phi\Omega + \tau^e - \tau^{int} + \tau_d - \mathcal{F}(\dot{q}^e)\right)
\end{aligned} \qquad (31)$$

By adding and subtracting the term $\xi_2^T \Phi\hat{\Omega}$ to the right-hand side of equation (31), the revised relation can be expressed as follows

$$\begin{aligned}
\dot{\mathcal{L}} = \dot{\mathcal{L}}_1 &+ \xi_2^T \Phi\hat{\Omega} + \xi_2^T \Phi\tilde{\Omega} + \xi_2^T\left(\tau^e - \tau^{int} + \tau_d - \mathcal{F}(\dot{q}^e)\right) \\
&- \tilde{\Omega}^T\Pi^{-1}\dot{\hat{\Omega}}
\end{aligned} \qquad (32)$$

Applying the transpose of $\xi_2^T \Phi\tilde{\Omega}$, equation (32) can be rewritten as

$$\dot{\mathcal{L}} = \dot{\mathcal{L}}_1 + \xi_2^T \Phi \hat{\Omega} + \xi_2^T \big(\tau^e - \tau^{int} + \tau_d - \mathcal{F}(\dot{q}^e) \big)$$
$$+ \tilde{\Omega}^T (\Phi^T \xi_2 - \Pi^{-1} \dot{\hat{\Omega}}) \tag{33}$$

Now by selecting $\dot{\hat{\Omega}}$ as

$$\dot{\hat{\Omega}} = \Pi \Phi^T \xi_2 \tag{34}$$

and after substituting equations (34) and (21) into equation (33), one may get modified relation as below

$$\dot{\mathcal{L}} = \dot{\mathcal{L}}_1 + \xi_2^T \Phi \hat{\Omega} + \xi_2^T \big(\tau^e - \tau^{int} + \tau_d - \mathcal{F}(\dot{q}^e) \big)$$
$$= -\xi_1^T \epsilon_1 \xi_1 + \xi_1^T \xi_2 + \xi_2^T \Phi \hat{\Omega} + \xi_2^T \tau^e - \xi_2^T \tau^{int}$$
$$+ \xi_2^T \tau_d - \xi_2^T \mathcal{F}(\dot{q}^e) \tag{35}$$

Employing the assumption (A) (equation (10)) and exploiting Young's inequality, the last term on the right-hand side of the equation (35) can be formulated as follows

$$\xi_2^T \tau_d \leqslant \frac{1}{2} \xi_2^T \xi_2 + \frac{1}{2} \tau_d^T \tau_d$$
$$\leqslant \frac{1}{2} \xi_2^T \xi_2 + \frac{1}{2} \bar{\tau}_d^2 \tag{36}$$

Thereafter, Lyapunov's derivative suffices the following inequality as

$$\dot{\mathcal{L}} = -\xi_1^T \epsilon_1 \xi_1 + \xi_1^T \xi_2 + \xi_2^T \Phi \hat{\Omega} + \xi_2^T \tau^e$$
$$- \xi_2^T \tau^{int} - \xi_2^T \mathcal{F}(\dot{q}^e) + \frac{1}{2} \xi_2^T \xi_2 + \frac{1}{2} \bar{\tau}_d^2 \tag{37}$$

Now, the trajectory tracking control law can be articulated as follows

$$\tau^e = -\epsilon_2 \xi_2 - \xi_1 - \Phi \hat{\Omega} - \frac{1}{2} \xi_2 + \tau^{int} + \mathcal{F}(\dot{q}^e) \tag{38}$$

where ϵ_2 represents another diagonal matrix of positive value. Moving further and placing the position control law from equations (38) to (37), the derivative of the Lyapunov function can be reworked as follows

$$\dot{\mathcal{L}} \leqslant -\xi_1^T \epsilon_1 \xi_1 - \xi_2^T \epsilon_2 \xi_2 + \frac{1}{2} \bar{\tau}_d^2 \tag{39}$$

It is clear from equation (39) that the derivative of the Lyapunov function can be reinstated in the following form of inequality

$$\dot{\mathcal{L}} \leqslant -\mho \mathcal{L} + \rho \tag{40}$$

where

$$\mho = \min \left(2\lambda_{\min}(\epsilon_1), \frac{2\lambda_{\min}(\epsilon_2)}{\lambda_{\max}(\mathcal{M}^e(q^e))} \right) \text{and} \quad \rho = \frac{1}{2} \bar{\tau}_d^2 \tag{41}$$

Here, ρ belongs to a class of κ functions and $\lambda_{min}(.), \lambda_{max}(.)$ denote the minimum and maximum eigenvalues of (.), respectively.

Multiplying the exponent term $e^{\mho t}$ to both sides of equation (40) and integrating for $t = [0, t]$ offers the equation as follows

$$0 \leqslant \mathcal{L} \leqslant \left(\mathcal{L}(0) - \frac{\rho}{\mho} \right) e^{-\mho t} + \frac{\rho}{\mho} \tag{42}$$

By defining $\widehat{\mathcal{L}} = \max\{\mathcal{L}(0), (\rho/\mho)\}$, two following inequalities can be obtained

$$\|\xi_1\| \leqslant \sqrt{2\widehat{\mathcal{L}}}, \text{ and } \quad \|\xi_2\| \leqslant \sqrt{\frac{2\widehat{\mathcal{L}}}{\lambda_{\max}(\mathcal{M}^e(q^e))}} \tag{43}$$

Remark 1. It is noticed from equations (42) and (43) that raising the $\mho$ and reducing the ρ can ensure the convergence of error signals $\|\xi_1\|$ and $\|\xi_2\|$ to small values. Consequently, the tracking performance with minimum permissible error can be augmented subject to the increasing value of controller gains ϵ_1 and ϵ_2. However, elevating the adaptation parameter Π ensures the rapid convergence of the estimated unknown parameters to the actual values. However, very large control parameters cannot be selected in real scenarios due to the noise and high frequency.

The above set of equations validates the characterization of input to state stability (ISS) where external disturbances τ_d refer to the bounded input, and thereby, the proposed tracking control guarantees the ultimate boundedness of all the signals.[48] Moreover, the congregation of even minor tracking errors for the coupled system can be ensured only using appropriate control law parameters.

Remark 2. The issue of "overparameterization" in the parametric strict-feedback system persists when the number of approximation parameters exceeds the number of unknown parameters. This occurrence results from the incoming unknown parameter estimates at each step of the adaptive backstepping approach. However, in this study, the initial step is specifically devised to avoid estimating unknown parameters and instead defers such estimations to the final step (Step 2), effectively overcoming the "overparameterization" problem. In addition, the problem of the "explosion of terms" is another widely recognized challenge arising

from the inclusion of inertia, centrifugal, and gravity derivative forms during the differentiation of the virtual control. Nevertheless, the proposed controller design in this work is devoid of such complexity, as it does not involve these dynamic matrices, thus mitigating the issue of the "explosion of terms" (refer to equation (23)).

Results and discussions

The simulation results of the proposed human-cooperative control strategy are demonstrated for two admittance levels; Case-I: AA with low-level admittance and Case-II: AA with high-level admittance. A block-wise architecture of the cooperative control strategy is illustrated in Figure 4. At first, the physiotherapist examines the desired gait trajectory obtained from the MOCAP setup and then allows implementation of the same for the human-cooperative control. Invoking the dynamic model given in Appendix 1, a trajectory tracking control law is designed with subject–exoskeleton interaction in MATLAB/Simulink (R2020b). An ode45 solver with variable step and non-adaptive zero crossing algorithm is exploited for different simulation runs. The potential of the proposed control strategy for both cases is examined using performance metrics, such as root mean square value (RMS) and maximum absolute value (MAX), depending on the results. These metrics can be expressed as follows

$$\text{RMS(P)} = \sqrt{\frac{1}{N} \sum_{v=1}^{N} p^2} \qquad (44)$$

where p denotes the performance parameter such that if p: the joint angular difference between human and reference trajectory, then RMS(P) denotes the root mean square difference (RMSD), and if p: joint angular error (ξ_1), then RMS(P) denotes the root mean square error (RMSE); N represents the total number of data points

$$\text{MAX(V)} = \max|v| \qquad (45)$$

where v denotes the performance value such that if v: interaction torque between human and exoskeleton, then MAX(V) denotes the maximum absolute interaction torque (MAXINTT), and if v: joint torque (τ^e), then MAX(V) signifies the maximum absolute joint torque (MAXJT).

At last, the effectiveness of the proposed cooperative control is compared with the contrast control, VSAR-HCC, given in Shen et al.[32] The reasons for selecting VSAR-HCC as contrast control are threefold: first, they have carried out an extensive study on the robust human-cooperative control with variable admittance models similar to the present work; second, they have also considered the sagittal plane with 3-DOFs (hip–
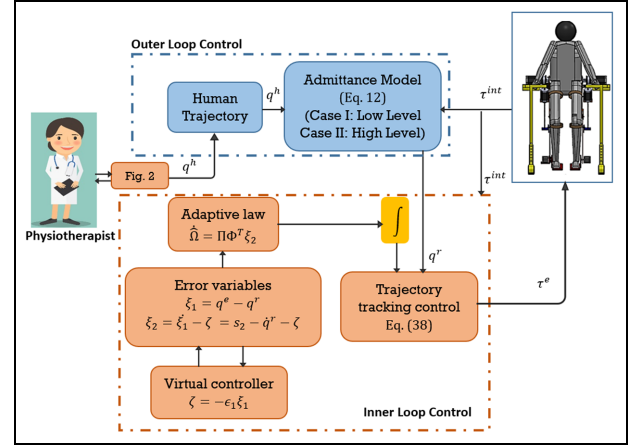

Figure 4. Schematic representation of proposed human-cooperative control.

knee–ankle); and third, the performance metrics used in present work are closely inline with them. The overall performance of the proposed cooperative control is examined using the percentage improvement factor (PIF), as defined below

$$\text{PIF} = \frac{\text{RMSE}_{VSAR-HCC} - \text{RMSE}_{RAB-HCC}}{\text{RMSE}_{VSAR-HCC}} \times 100\% \qquad (46)$$

where $\text{RMSE}_{RAB-HCC}$ and $\text{RMSE}_{VSAR-HCC}$ represent the RMSE for proposed and contrast control, respectively.

In both control approaches, the coupled human–exoskeleton mass of lower-limb segments is increased by 30%, 20%, and 10% ($m_1^{(e,h)} = m_1^{(e,h)} + 0.3m_1^{(e,h)}$, $m_2^{(e,h)} = m_2^{(e,h)} + 0.2m_2^{(e,h)}, m_3^{(e,h)} = m_3^{(e,h)} + 0.1m_3^{(e,h)}$) to induce the parametric uncertainties, respectively. The external interferences are considered as $\tau_{d(hip)} = 6 \sin(2t) + \text{random}(1), \tau_{d(knee)} = 4\sin(t) + 2 \times \text{random}(1)$, $\tau_{d(ankle)} = 2\sin(t)$. In this work, a periodic (sinusoidal) form of external disturbances is added to mimic the effect of sudden reflexes induced at the joints throughout a gait cycle. The damping and spring constant factors for the bracing straps in equation (5) are selected as $c = [10, 10, 2]^T$ and $k = [200, 200, 20]^T$. Performing numerical iterations based on Remark 1, the parameters of a robust trajectory control scheme are selected as $\epsilon_1 = \text{diag}(120, 55, 55)$, $\epsilon_2 = \text{diag}(10, 25, 25)$, and $\Pi = 0.1$. The Coulomb friction and velocity factor are considered as $C_f = [0.8, 0.8, 0.8]^T$ and $\sigma = [1.2, 1.2, 1.2]^T$, respectively.

For Case-I (low admittance level), the values of admittance parameters are selected as $M_a = \text{diag}(7, 7, 7)$, $C_a = \text{diag}(2, 2, 2)$, and $K_a = \text{diag}(50, 50, 50)$. However, the admittance values for Case-II (high admittance level) is chosen as $M_a = \text{diag}(12, 12, 12)$, $C_a = \text{diag}(6, 6, 6)$, and $K_a = \text{diag}(200, 200, 200)$. Incorporating the inner- and outer-
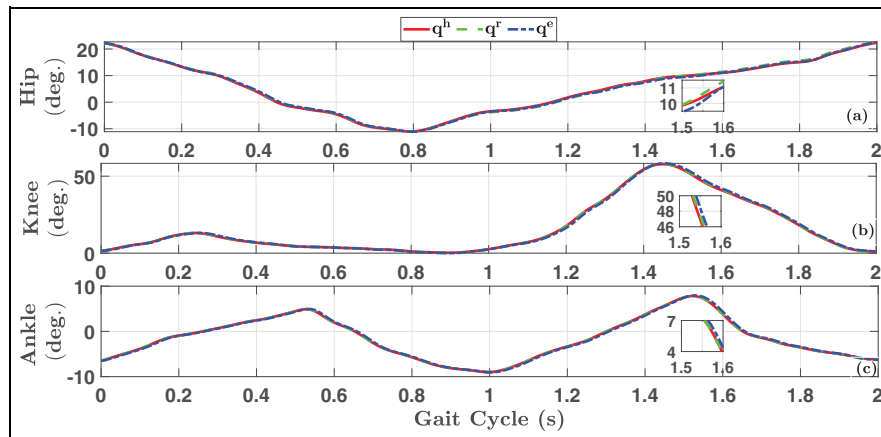
Figure 5. Trajectory tracking with low admittance parameters for (a) hip, (b) knee, and (c) ankle joint.
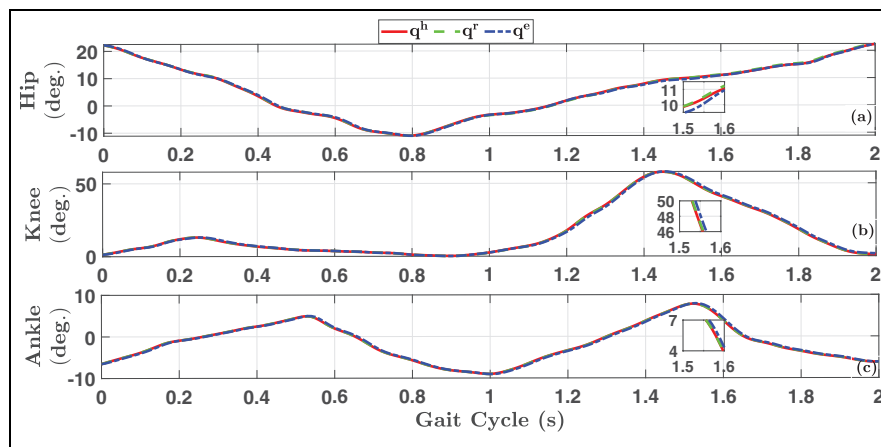

Figure 6. Trajectory tracking with high admittance parameters for (a) hip, (b) knee, and (c) ankle joint.

loop control parameters, the desired (q^h), reference (q^r), and actual (q^e) joint trajectory for Case-I and Case-II is presented in Figures 5(a)–(c) and 6(a)–(c), respectively. As per the motion capture experiment, a gait cycle of 2 s is considered for all the co-simulation runs. A zoom-in view at ($X: 1.5, 1.6; Y: 9.5, 11.7$), ($X: 1.5, 1.6; Y: 45.9, 50.05$), and ($X: 1.5, 1.6; Y: 4.01, 7.05$) is shown for hip, knee, and ankle joint movement in both cases.

Invoking the joint tracking results from Figures 5 and 6, the actual Cartesian gait trajectory tracked by exoskeleton with low and high admittance levels is shown in Figure 7. Three zoom-in views with ($X: -0.123, -0.114; Y: -0.5896, -0.5873$), ($X: 0.34, 0.36; Y: -0.41, -0.39$), and ($X: 0.2, 0.2235; Y: -0.565, -0.55$), shown at three respective secondary axes, ensures the preliminary idea of more active participation of the subject in case of low admittance levels. However, for more clarity, the difference between desired and reference trajectory ($q^h - q^r$) and the error between actual and reference trajectory ($q^e - q^r$) are presented and discussed further.

The disparity in desired and reference trajectory ($q^h - q^r$) for both cases is shown in Figure 8. The reference one (q^r) depends on interaction torques and the required admittance level. It is evident from Figure 8(a) that the difference for the hip joint is more significant with low-level admittance (RMSD: $0.309°$) as compared to the high-level admittance (RMSD: $0.159°$). Likewise, a trend is noticed for the knee joint, as seen in Figure 8(b). As interpreted from Figure 8(c) and Table 2, a reverse trend is observed for the ankle joint with a marginal deviation between two admittance levels. Such trends suggest that the exoskeleton system enables the subject to participate more freely in Case-I over Case-II. The error in reference and actual trajectory ($q^e - q^r$) for each lower-limb joint is shown in Figure 9(a)–(c). Further investigating the effectiveness of the robust adaptive backstepping tracking control, the exoskeleton system follows the reference trajectory more precisely with Case-II (RMSE$_{hip}$: $0.227°$, RMSE$_{knee}$: $0.512°$, RMSE$_{ankle}$: $0.179°$) as compared to Case-I (RMSE$_{hip}$: $0.246°$, RMSE$_{knee}$: $0.519°$, RMSE$_{ankle}$: $0.181°$). Although there is marginal variation in the
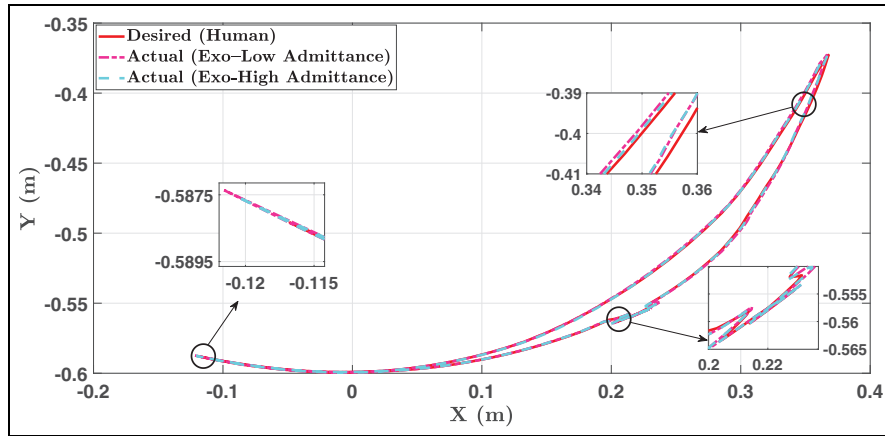
Figure 7. Actual Cartesian trajectory tracked by exoskeleton in low and high admittance mode.
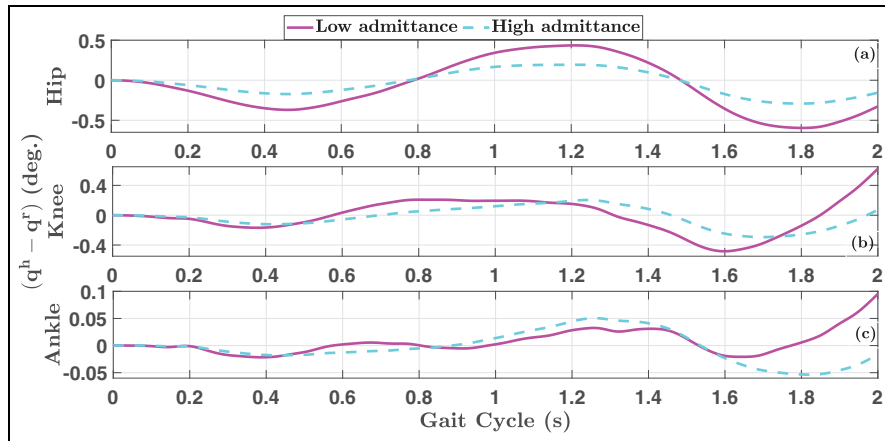

Figure 8. Difference between desired (human) and reference trajectory for (a) hip, (b) knee, and (c) ankle joint.
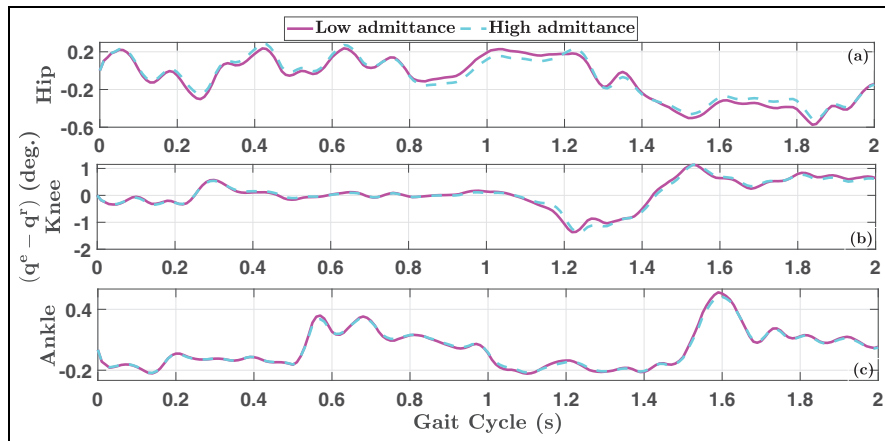

Figure 9. Difference between reference and actual trajectory for (a) hip, (b) knee, and (c) ankle joint.

RMSE of the knee and ankle joint for both cases, it can be deduced from Table 2 that the proposed trajectory control is a little less promising for tracking the reference gait when the subject is cooperating more frankly.

Following the adaptation law (equation (34)), the estimation of the unknown parameters for the exoskeleton system with low- and high-level admittance is shown in Figures 10 and 11. Although, in both cases, the estimated parameters are bounded and converged

Table 2. Comparative performance analysis of the proposed cooperative control.

Admittance	Performance(° or Nm)	Hip	Knee	Ankle
Case I: Low level	RMSD	0.309	0.183	0.021
	RMSE	0.246	0.519	0.181
	MAXINTT	13.07	29.61	5.04
	MAXJT	152.07	68.63	7.34
Case II: High level	RMSD	0.159	0.141	0.028
	RMSE	0.227	0.512	0.179
	MAXINTT	10.55	28.09	4.98
	MAXJT	171.80	86.67	8.33

RMSD: root mean square difference; RMSE: root mean square error; MAXINTT: maximum absolute interaction torque; MAXJT: maximum absolute joint torque.
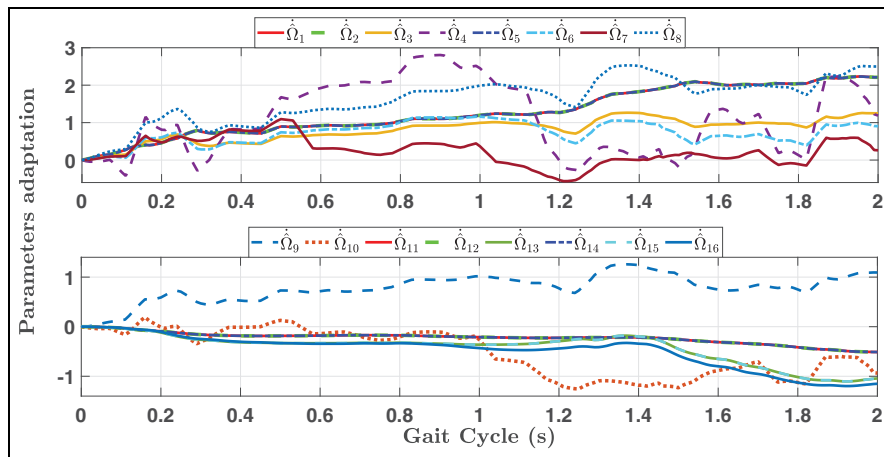

Figure 10. Parameter adaptation of Ω for the coupled human–exoskeleton system in low admittance mode.
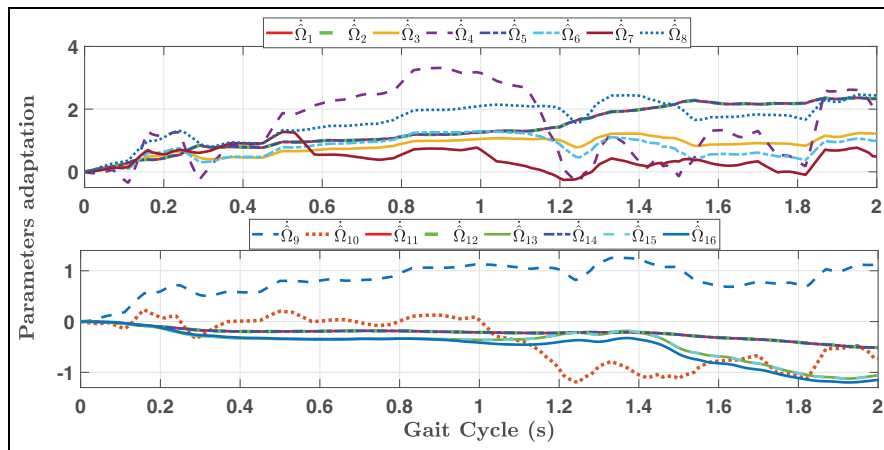

Figure 11. Parameter adaptation of Ω for the coupled human–exoskeleton system in high admittance mode.

to preserve the stability of the closed-loop process with promising gait tracking performance; however, the confluence of these parameters to their true values is not compulsorily possible. Furthermore, it can be noted from the results of both cases that estimation of 1st, 2nd, and 5th parameters ($\dot{\hat{\Omega}}_1, \dot{\hat{\Omega}}_2, \dot{\hat{\Omega}}_5$) follows same

adaptation over the gait cycle. Likewise, the 11th, 12th, and 14th parameters ($\dot{\hat{\Omega}}_{11}, \dot{\hat{\Omega}}_{12}, \dot{\hat{\Omega}}_{14}$) are estimated with same adaptation values. Moreover, the 13th estimated parameter ($\dot{\hat{\Omega}}_{13}$) converges with the same values as of 15th parameter ($\dot{\hat{\Omega}}_{15}$). These
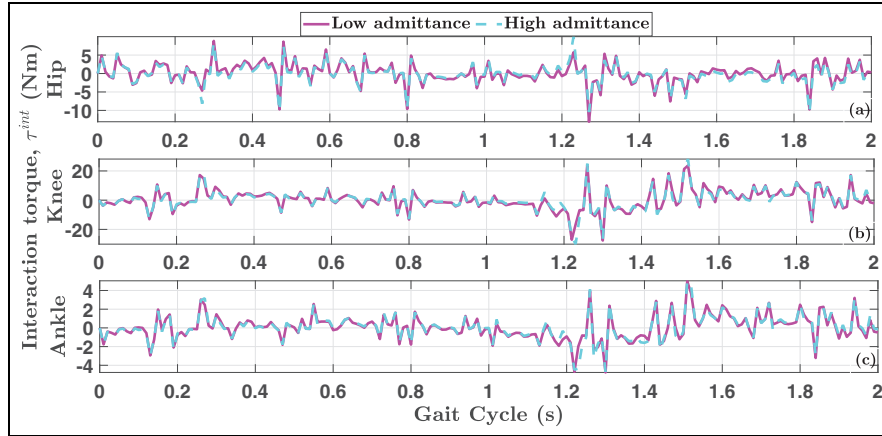
Figure 12. Interaction torques over a gait cycle for (a) hip, (b) knee, and (c) ankle joint.
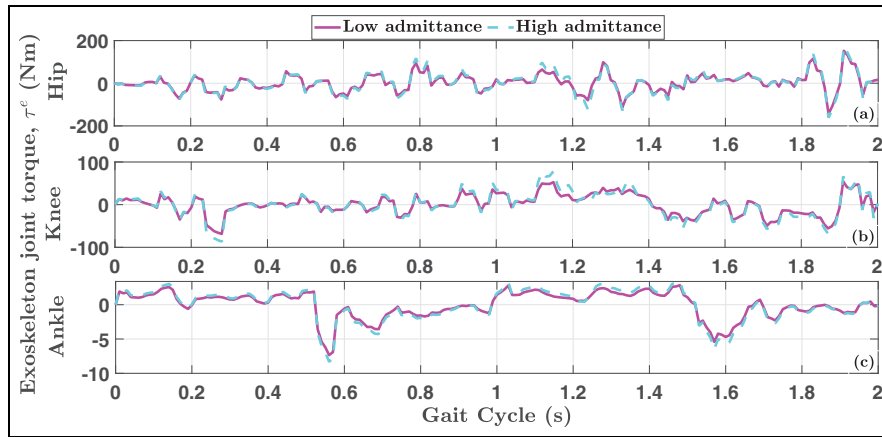

Figure 13. Control torques over a gait cycle for (a) hip, (b) knee, and (c) ankle joint.

observations show that the number of parameter estimates ($n_{\hat{\Omega}} = 11$) are less than the number of unknown parameters ($n_{\Omega} = 16$), which further supports the Remark 1 of avoiding "overparameterization" phenomena.

The interaction torque (τ^{int}) produced for the hip, knee, and ankle joint is displayed in Figure 12(a)–(c). At most of the gait cycle, these interaction torques exceed for Case-I as compared to Case-II and comply with the more considerable difference between desired and reference joint trajectories in case of low admittance values (refer Figure 8). Moreover, it is evident from Table 2 that the MAXINTT for every lower-limb joint is higher in Case-I compared to the corresponding MAXINTT of Case-II. However, referring Figure 13(a)–(c) for joint torque (τ^e), it is worth noting that maximum joint torque for each joint is lesser for Case-I (MAXJT$_{hip}$: 152.07 Nm, MAXJT$_{knee}$: 68.63 Nm, and MAXJT$_{ankle}$: 7.34 Nm) as compared to the Case-II (MAXJT$_{hip}$: 171.80 Nm, MAXJT$_{knee}$: 86.67 Nm, and MAXJT$_{ankle}$: 8.33 Nm) which implies augmented participation of subject's muscle strength. Therefore, when the pediatric subject can exert force from the side with

considerable limb flexibility, actuators with less torque capacity will be needed in the exoskeleton design for tracking the reference trajectory.

The effectiveness of the proposed RAB-HCC control is now validated by comparing it with contrast control, that is, VSAR-HCC. The trajectory error ($q^e - q^r$) for hip, knee, and ankle joints in low- and high-level admittance is shown in Figures 14 and 15. For both cases, it can be clearly noticed from Table 3 that the proposed cooperative control with the RAB technique outperforms the contrast cooperative control with the VSAR method (Case-I: PIF$_{hip}$: 63.82%, PIF$_{knee}$: 45.15%, and PIF$_{ankle}$: 33.21%; Case-II: PIF$_{hip}$: 61.78%, PIF$_{knee}$: 50.24%, and PIF$_{ankle}$: 34.67%). The PIF is increased by 2.04% for the hip joint, decreased by 5.09% for the knee joint, and reduced by 1.56% for the ankle joint while comparing the results of Case-I over Case-II. The detailed performance analysis is presented in Table 3.

Finally, it can be interpreted from the above observations that the proposed human-cooperative control with low-level admittance is more advantageous for subjects who have partially regained their muscle
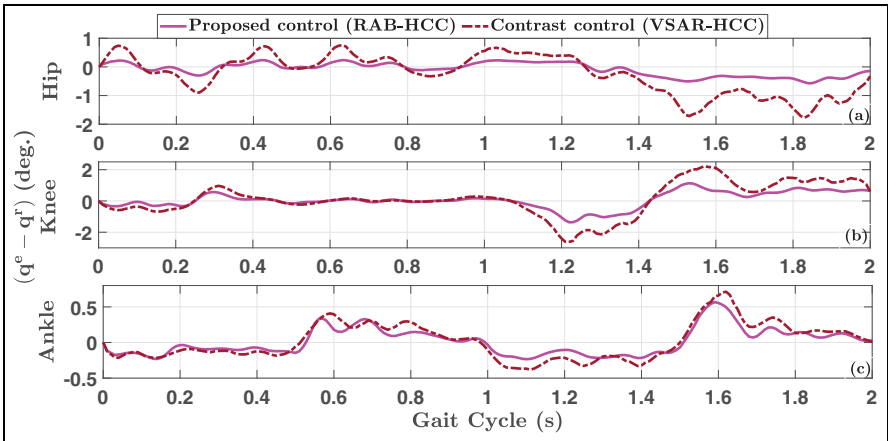
Figure 14. Comparative estimation of error ($q^e - q^r$) for (a) hip, (b) knee, and (c) ankle joint with proposed (RAB-HCC) and contrast control (VSAR-HCC) with low-level admittance.
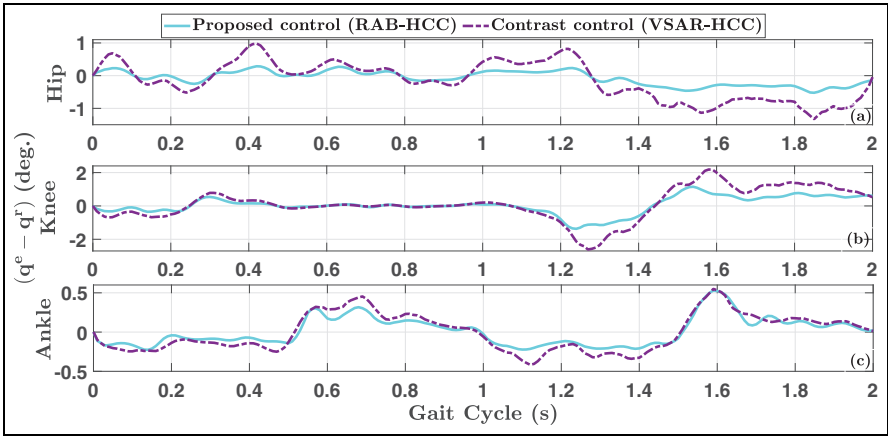

Figure 15. Comparative estimation of error ($q^e - q^r$) for (a) hip, (b) knee, and (c) ankle joint with proposed (RAB-HCC) and contrast control (VSAR-HCC) with high-level admittance.

Table 3. Comparative performance analysis of the proposed control over the contrast control during the AA rehabilitation.

Joint	Case-I: Low-level admittance (RMSE, °)		PIF (%)	Case-II: High-level admittance (RMSE, °)		PIF (%)
	Contrast control (VSAR-HCC)	Proposed control (RAB-HCC)		Contrast control (VSAR-HCC)	Proposed control (RAB-HCC)	
Hip	0.680	0.246	63.82	0.594	0.227	61.78
Knee	0.939	0.515	45.15	1.029	0.512	50.24
Ankle	0.271	0.181	33.21	0.274	0.179	34.67

RMSE: root mean square error; PIF: percentage improvement factor; VSAR-HCC: variable structure adaptive robust-based human-cooperative control; RAB-HCC: robust adaptive backstepping human-cooperative control.

strength while recovering from a neurological disorder and requires less assistance from the exoskeleton system. Contrariwise, the human-cooperative control with high-level admittance is helpful for subjects in the initial phases of recovery and carrying minimal residual strength in their lower-limb muscles. Such subjects cannot actively participate compared to the subjects with partial recovery, thereby diverging less from the healthy human trajectory. In the cases mentioned above, the reference trajectory is effectively tracked by the actual one using a robust ABC under parametric uncertainties and external disturbances. However, low- and high-level admittance values in the proposed control should be attentively selected to establish the safety aspects of the user by allowing them to move joints within maximum ROMs.

Conclusion

This work has proposed a novel human-cooperative control framework of a pediatric exoskeleton to regulate human participation during AA rehabilitation. Initially, the design and modeling of the exoskeleton system have been briefly presented. Thereafter, an admittance model as outer-loop control and a trajectory tracking scheme as inner-loop control have been formulated. For tracking reference gait trajectory in the inner loop, a robust ABC has been introduced to deal with parametric uncertainties and external perturbations. The proposed tracking control has been designed through appropriate Lyapunov functions and avoided the controller's complexities. The performance of the proposed cooperative control has been studied under low- and high-level admittance modes. Moreover, the effectiveness of the proposed control (RAB-HCC) has been validated with a contrast control (VSAR-HCC). From the co-simulation runs, it has been factually observed that RAB-HCC allows the subject to participate more frankly in low admittance mode. While tracking the reference trajectory, RAB-HCC outperforms the VSAR-HCC in both admittance modes.

ORCID iDs

Jyotindra Narayan (iD) https://orcid.org/0000-0002-2499-6039
Bhaben Kalita (iD) https://orcid.org/0000-0001-8361-9308

References

1. Feigin VL, Vos T, Alahdab F, et al. Burden of neurological disorders across the US from 1990-2017: a global burden of disease study. *JAMA Neurol* 2021; 78(2): 165–176.
2. Meyer S, Poryo M, Flotats-Bastardas M, et al. Schlaganfall bei kindern und jugendlichen. *Radiologe* 2017; 57(7): 569–576.
3. Chauhan A, Singh M, Jaiswal N, et al. Prevalence of cerebral palsy in Indian children: a systematic review and meta-analysis. *Indian J Pediatr* 2019; 86(12): 1124–1130.
4. Smania N, Bonetti P, Gandolfi M, et al. Improved gait after repetitive locomotor training in children with cerebral palsy. *Am J Phys Med Rehab* 2011; 90(2): 137–149.
5. De Sousa DG, Harvey LA, Dorsch S, et al. Interventions involving repetitive practice improve strength after stroke: a systematic review. *J Physiother* 2018; 64(4): 210–221.
6. Kalita B, Narayan J and Dwivedy SK. Development of active lower limb robotic-based orthosis and exoskeleton devices: a systematic review. *Int J Soc Robot* 2021; 13(4): 775–793.
7. Narayan J, Kalita B and Dwivedy SK. Development of robot-based upper limb devices for rehabilitation purposes: a systematic review. *Augment Hum Res* 2021; 6(1): 4.
8. Hassani W, Mohammed S, Rifaï H, et al. Powered orthosis for lower limb movements assistance and rehabilitation. *Control Eng Pract* 2014; 26: 245–253.
9. Tu Y, Zhu A, Song J, et al. An adaptive sliding mode variable admittance control method for lower limb rehabilitation exoskeleton robot. *Appl Sci* 2020; 10(7): 2536.
10. Yang J and Peng C. Adaptive motion intent understanding–based control of human–exoskeleton system. *Proc IMechE, Part I: J Systems and Control Engineering* 2021; 235(2): 180–189.
11. Kazerooni H, Steger R and Huang L. Hybrid control of the Berkeley Lower Extremity Exoskeleton (BLEEX). *Int J Robot Res* 2006; 25(5–6): 561–573.
12. Taherifar A, Vossoughi G and Ghafari AS. Variable admittance control of the exoskeleton for gait rehabilitation based on a novel strength metric. *Robotica* 2018; 36(3): 427–447.
13. Ajayi MO, Djouani K and Hamam Y. Bounded control of an actuated lower-limb exoskeleton. *J Robot* 2017; 2017: 2423643.
14. Wang Y, Wang H and Tian Y. Nonlinear disturbance observer based flexible-boundary prescribed performance control for a lower limb exoskeleton. *Int J Syst Sci* 2021; 52(15): 3176–3189.
15. Al Rezage G and Tokhi MO. Fuzzy PID control of lower limb exoskeleton for elderly mobility. In: *Proceedings of the 2016 IEEE international conference on automation, quality and testing, robotics (AQTR)*, Cluj-Napoca, 19–21 May 2016, pp.1–6. New York: IEEE.
16. Amiri MS, Ramli R and Ibrahim MF. Hybrid design of PID controller for four DoF lower limb exoskeleton. *Appl Math Model* 2019; 72: 17–27.
17. Wang J, Liu J, Chen L, et al. Observer-based finite-time control for trajectory tracking of lower extremity exoskeleton. *Proc IMechE, Part I: J Systems and Control Engineering* 2022; 236(2): 257–269.
18. Mokhtari M, Taghizadeh M and Mazare M. Hybrid adaptive robust control based on CPG and ZMP for a lower limb exoskeleton. *Robotica* 2021; 39(2): 181–199.
19. Narayan J and Dwivedy SK. Robust LQR-based neural-fuzzy tracking control for a lower limb exoskeleton system with parametric uncertainties and external disturbances. *Appl Bionics Biomech* 2021; 2021: 5573041.
20. Narayan J, Abbas M and Dwivedy SK. Adaptive iterative learning-based gait tracking control for paediatric

exoskeleton during passive-assist rehabilitation. *Int J Intell Eng Informat* 2021; 9(6): 507–532.

21. Hasan SK and Dhingra AK. Development of a model reference computed torque controller for a human lower extremity exoskeleton robot. *Proc IMechE, Part I: J Systems and Control Engineering* 2021; 235(9): 1615–1637.

22. Narayan J, Abbas M, Patel B, et al. A singularity-free terminal sliding mode control of an uncertain paediatric exoskeleton system. In: *Proceedings of the 2022 5th international conference on advanced systems and emergent technologies (IC_ASET)*, Hammamet, 22–25 March 2022, pp.198–203. New York: IEEE.

23. Vallery H, Duschau-Wicke A and Riener R. Generalized elasticities improve patient-cooperative control of rehabilitation robots. In: *Proceedings of the 2009 IEEE international conference on rehabilitation robotics*, Kyoto, Japan, 23–26 June 2009, pp.535–541. New York: IEEE.

24. Saglia JA, Tsagarakis NG, Dai JS, et al. Control strategies for patient-assisted training using the ankle rehabilitation robot (ARBOT). *IEEE/ASME T Mech* 2012; 18(6): 1799–1808.

25. Ayas MS and Altas IH. A redundantly actuated ankle rehabilitation robot and its control strategies. In: *Proceedings of the 2016 IEEE symposium series on computational intelligence (SSCI)*, Athens, 6–9 December 2016, pp.1–7. New York: IEEE.

26. Luo R, Sun S, Zhao X, et al. Adaptive CPG-based impedance control for assistive lower limb exoskeleton. In: *Proceedings of the 2018 IEEE international conference on robotics and biomimetics (ROBIO)*, Kuala Lumpur, Malaysia, 12–15 December 2018, pp.685–690. New York: IEEE.

27. He Y, Eguren D, Azorín JM, et al. Brain–machine interfaces for controlling lower-limb powered robotic systems. *J Neural Eng* 2018; 15(2): 021004.

28. Torabi M, Sharifi M and Vossoughi GR. Robust adaptive sliding mode admittance control of exoskeleton rehabilitation robots. *Sci Iran* 2018; 25(5): 2628–2642.

29. Almaghout K, Tarvirdizadeh B, Alipour K, et al. Design and control of a lower limb rehabilitation robot considering undesirable torques of the patient's limb. *Proc IMechE, Part H: J Engineering in Medicine* 2020; 234(12): 1457–1471.

30. Mokhtari M, Taghizadeh M and Mazare M. Impedance control based on optimal adaptive high order super twisting sliding mode for a 7-DOF lower limb exoskeleton. *Meccanica* 2021; 56(3): 535–548.

31. Zhang X, Yin G, Li H, et al. An adaptive seamless assist-as-needed control scheme for lower extremity rehabilitation robots. *Proc IMechE, Part I: J Systems and Control Engineering* 2021; 235(6): 723–734.

32. Shen Z, Zhuang Y, Zhou J, et al. Design and test of admittance control with inner adaptive robust position control for a lower limb rehabilitation robot. *Int J Control Autom* 2020; 18(1): 134–142.

33. Zhou J and Wen C. *Adaptive backstepping control of uncertain systems: nonsmooth nonlinearities, interactions or time-variations*. Berlin; Heidelberg: Springer, 2008.

34. Vaidyanathan S and Azar AT. *Backstepping control of nonlinear dynamical systems*. Cambridge, MA: Academic Press, 2020.

35. Zhang Y, Chen WH and Soh YC. Improved robust backstepping adaptive control for nonlinear discrete-time systems without overparameterization. *Automatica* 2008; 44(3): 864–867.

36. Guo Q, Zhang Y, Celler BG, et al. Neural adaptive backstepping control of a robotic manipulator with prescribed performance constraint. *IEEE T Neur Net Lear* 2019; 30(12): 3572–3583.

37. Adhikary N and Mahanta C. Backstepping sliding mode controller for a co-ordinated links (COOL) robot arm. In: *Proceedings of the 2014 13th international workshop on variable structure systems (VSS)*, Nantes, 29 June–2 July 2014, pp.1–5. New York: IEEE.

38. Shi X, Cheng Y, Yin C, et al. Design of adaptive backstepping dynamic surface control method with RBF neural network for uncertain nonlinear system. *Neurocomputing* 2019; 330: 490–503.

39. Zhou C, Li C, Song Y, et al. Optimal design and command filtered backstepping control of exoskeleton with series elastic actuator. *J Dyn Syst: T ASME* 2022; 144: 091002.

40. Narayan J and Dwivedy SK. Preliminary design and development of a low-cost lower-limb exoskeleton system for paediatric rehabilitation. *Proc IMechE, Part H: J Engineering in Medicine* 2021; 235(5): 530–545.

41. Narayan J, Bhoir AA, Borgohain A, et al. Design and analysis of a stand-aided lower-limb exoskeleton system for pediatric rehabilitation. In: *Proceedings of the 2021 international conference on computational performance evaluation (ComPE)*, Shillong, India, 1–3 December 2021, pp.950–955. New York: IEEE.

42. Narayan J and Dwivedy SK. Towards neuro-fuzzy compensated PID control of lower extremity exoskeleton system for passive gait rehabilitation. *IETE J Res* 2023; 69: 778–795.

43. Chester VL, Tingley M and Biden EN. A comparison of kinetic gait parameters for 3–13 year olds. *Clin Biomech* 2006; 21(7): 726–732.

44. Cigali BS, Uluçam E and Bozer C. 3D motion analysis of hip, knee and ankle joints of children aged between 7-11 years during gait. *Balk Med J* 2011; 28(2): 197–201.

45. Narayan J and Dwivedy SK. Biomechanical study and prediction of lower extremity joint movements using bayesian regularization-based backpropagation neural network. *J Comput Inf Sci Eng* 2022; 22(1): 014503.

46. Spong MW, Hutchinson S, Vidyasagar M, et al. *Robot modeling and control*, vol. 3. New York: Wiley, 2006.

47. Abbas M, Narayan J and Dwivedy SK. Event-triggered adaptive control for upper-limb robot-assisted passive rehabilitation exercises with input delay. *Proc IMechE, Part I: J Systems and Control Engineering* 2022; 236(4): 832–845.

48. Liu T, Zhang P and Jiang ZP. Event-triggered input-to-state stabilization of nonlinear systems subject to disturbances and dynamic uncertainties. *Automatica* 2019; 108: 108488.

Appendix 1

The element-wise expression of inertia, Coriolis/centrifugal, and gravity matrix for the exoskeleton simulation is as follows

$$\mathcal{M}^e(q^e) = \begin{bmatrix} \mathcal{M}^e_{11} & \mathcal{M}^e_{12} & \mathcal{M}^e_{13} \\ \mathcal{M}^e_{21} & \mathcal{M}^e_{22} & \mathcal{M}^e_{23} \\ \mathcal{M}^e_{31} & \mathcal{M}^e_{32} & \mathcal{M}^e_{33} \end{bmatrix},$$

$$\mathcal{C}^e(q^e, \dot{q}^e) = \begin{bmatrix} \mathcal{C}^e_{11} & \mathcal{C}^e_{12} & \mathcal{C}^e_{13} \\ \mathcal{C}^e_{21} & \mathcal{C}^e_{22} & \mathcal{C}^e_{23} \\ \mathcal{C}^e_{31} & \mathcal{C}^e_{32} & \mathcal{C}^e_{33} \end{bmatrix}, \mathcal{G}^e(q^e) = \begin{bmatrix} \mathcal{G}^e_1 \\ \mathcal{G}^e_2 \\ \mathcal{G}^e_3 \end{bmatrix}$$

$$\mathcal{M}^e_{11} = m^e_1 l^{e2}_{c1} + I^e_1 + m^e_2(l^{e2}_1 + l^{e2}_{c2} + 2l^e_1 l^e_{c2} \cos q^e_2)$$
$$+ I^e_2 + m^e_3(l^{e2}_1 + l^{e2}_2 + l^{e2}_{c3} + 2l^e_1 l^e_2 \cos q^e_2$$
$$+ 2l^e_1 l^e_{c3} \cos q^e_{23}) + I^e_3$$

$$\mathcal{M}^e_{12} = m^e_2(l^{e2}_{c2} + l^e_1 l^e_{c2} \cos q^e_2) + I^e_2 + m^e_3(l^{e2}_2 + l^{e2}_{c3}$$
$$+ l^e_1 l^e_2 \cos q^e_2 + l^e_1 l^e_{c3} \cos q^e_{23} + 2l^e_2 l^e_{c3} \cos q^e_3) + I^e_3$$

$$\mathcal{M}^e_{13} = m^e_3(l^{e2}_{c3} + l^e_1 l^e_{c3} \cos q^e_{23} + l^e_2 l^e_{c3} \cos q^e_3) + I^e_3$$

$$\mathcal{M}^e_{22} = m^e_2 l^{e2}_{c2} + I^e_2 + m^e_3(l^{e2}_2 + l^{e2}_{c3} + 2l^e_2 l^e_{c3} \cos q^e_3) + I^e_3$$

$$\mathcal{M}^e_{23} = m^e_3(l^{e2}_{c3} + l^e_2 l^e_{c3} \cos q^e_3) + I^e_3$$

$$\mathcal{M}^e_{33} = m^e_3 l^{e2}_{c3} + I^e_3$$

$$\mathcal{M}^e_{21} = \mathcal{M}^e_{12}, \mathcal{M}^e_{13} = \mathcal{M}^e_{31}, \mathcal{M}^e_{23} = \mathcal{M}^e_{32}$$

$$\mathcal{C}^e_{11} = -2m^e_2 l^e_1 l^e_{c2} \sin q^e_2 \dot{q}^e_2 - 2m^e_3 l^e_1 l^e_2 \sin q^e_2 \dot{q}^e_2$$
$$- 2m^e_3 l^e_1 l^e_{c3} \sin q^e_{23}(\dot{q}^e_2 + \dot{q}^e_3) - 2m^e_3 l^e_2 l^e_{c3} \sin q^e_3 \dot{q}^e_3$$

$$\mathcal{C}^e_{12} = -m^e_2 l^e_1 l^e_{c2} \sin q^e_2(2\dot{q}^e_1 + \dot{q}^e_2)$$
$$- m^e_3 l^e_1 l^e_2 \sin q^e_2(2\dot{q}^e_1 + \dot{q}^e_2)$$
$$- m^e_3 l^e_1 l^e_{c3} \sin q^e_{23}(2\dot{q}^e_1 + \dot{q}^e_2 + \dot{q}^e_3)$$

$$\mathcal{C}^e_{13} = -m^e_3 l^e_1 l^e_{c3} \sin q^e_{23}(2\dot{q}^e_1 + 2\dot{q}^e_2 + \dot{q}^e_3)$$

$$\mathcal{C}^e_{21} = -2m^e_3 l^e_2 l^e_{c3} \sin q^e_3 \dot{q}^e_3 + (m^e_2 l^e_1 l^e_{c2} \sin q^e_2$$
$$+ m^e_3(l^e_1 l^e_2 \sin q^e_2 + l^e_1 l^e_{c3} \sin q^e_{23}))\dot{q}^e_1$$

$$\mathcal{C}^e_{22} = -2m^e_3 l^e_2 l^e_{c3} \sin q^e_3 \dot{q}^e_3$$

$$\mathcal{C}^e_{23} = -m^e_3 l^e_2 l^e_{c3} \sin q^e_3(2\dot{q}^e_1 + 2\dot{q}^e_2 + \dot{q}^e_3)$$

$$\mathcal{C}^e_{31} = m^e_3 l^e_1 l^e_{c3} \sin q^e_{23} \dot{q}^e_1 + m^e_3 l^e_2 l^e_{c3} \sin q^e_3(\dot{q}^e_1 + 2\dot{q}^e_2)$$

$$\mathcal{C}^e_{32} = m^e_3 l^e_2 l^e_{c3} \sin q^e_3(2\dot{q}^e_1 + \dot{q}^e_2)$$

$$\mathcal{C}^e_{33} = 0$$

$$\mathcal{G}^e_1 = m^e_1 g l^e_{c1} \sin q^e_1 + m^e_2 g(l^e_1 \sin q^e_1 + l^e_{c2} \sin q^e_{12})$$
$$+ m^e_3 g(l^e_1 \sin q^e_1 + l^e_2 \sin q^e_{12} + l^e_{c3} \sin q^e_{123})$$

$$\mathcal{G}^e_2 = m^e_2 g l^e_{c2} \sin q^e_{12} + m^e_3 g(l^e_2 \sin q^e_{12} + l^e_{c3} \sin q^e_{123})$$

$$\mathcal{G}^e_3 = m^e_3 g l^e_{c3} \sin q^e_{123}$$

In the above expressions, $I^e_i \quad \forall i = 1, 2, 3$ denotes the moment of inertia about the respective link of the exoskeleton system.

Appendix 2

The elements of the regression matrix ($\Phi \in \mathbb{R}^{3 \times 16}$) and the vector of unknown parameters ($\Omega \in \mathbb{R}^{16 \times 1}$) are as follows

$$\Phi(1, 1) = \Phi(1, 2) = \Phi(1, 5) = \ddot{q}^e_1,$$

$$\Phi(1, 3) = \ddot{q}^e_1 \cos q^e_2 + \frac{\cos q^e_2}{2}\ddot{q}^e_2 - \dot{q}^e_2 \dot{q}^e_1 \sin q^e_2$$
$$- (\sin q^e_2)\dot{q}^e_2\left(\dot{q}^e_1 + \frac{\dot{q}^e_2}{2}\right)$$

$$\Phi(1, 4) = \ddot{q}^e_1 + 4\ddot{q}^e_2, \quad \Phi(1, 6) = \ddot{q}^e_1 + \ddot{q}^e_2,$$

$$\Phi(1, 7) = \ddot{q}^e_1 + \ddot{q}^e_2 + \ddot{q}^e_3$$

$$\Phi(1, 8) = 2(\cos q^e_2)\ddot{q}^e_1 + (\cos q^e_2)\ddot{q}^e_2 - 4(\sin q^e_2)\dot{q}^e_2 \dot{q}^e_1$$
$$- (\sin q^e_2)(\dot{q}^e_2)^2$$

$$\Phi(1, 9) = (\cos q^e_{23})\ddot{q}^e_1 + \frac{(\cos q^e_{23})}{2}\ddot{q}^e_2 + \frac{(\cos q^e_{23})}{2}\ddot{q}^e_3$$
$$- 2(\sin q^e_{23})\dot{q}^e_2 \dot{q}^e_1 - 3\frac{(\sin q^e_{23})}{2}\dot{q}^e_3 \dot{q}^e_2$$
$$- 2(\sin q^e_{23})\dot{q}^e_1 \dot{q}^e_3$$
$$- \frac{(\sin q^e_{23})}{2}(\dot{q}^e_2)^2 - \frac{(\sin q^e_{23})}{2}(\dot{q}^e_3)^2$$

$$\Phi(1, 10) = (\cos q^e_3)\ddot{q}^e_2 + \frac{(\cos q^e_3)}{2}\ddot{q}^e_3,$$

$$\Phi(1, 11) = \Phi(1, 12) = \Phi(1, 14) = g \sin q^e_1,$$

$$\Phi(1, 13) = \Phi(1, 15) = g \sin q^e_{12}, \quad \Phi(1, 16) = g \sin q^e_{123}$$

$$\Phi(2, 1) = \Phi(2, 2) = \Phi(2, 5)$$
$$= \Phi(2, 11) = \Phi(2, 12) = \Phi(2, 14) = 0$$

$$\Phi(2, 3) = \frac{(\sin q^e_2)}{2}(\dot{q}^e_1)^2, \quad \Phi(2, 4) = 4\ddot{q}^e_2,$$

$$\Phi(2, 6) = \frac{\ddot{q}^e_2}{2}, \quad \Phi(2, 7) = \ddot{q}^e_2 + \ddot{q}^e_2$$

$$\Phi(2, 8) = (\sin q^e_2)(\dot{q}^e_1)^2, \quad \Phi(2, 9) = \frac{(\sin q^e_{23})}{2}(\dot{q}^e_1)^2$$

$$\Phi(2, 10) = (\cos q^e_3)(\ddot{q}^e_2 + \ddot{q}^e_3) - 2(\sin q^e_3)\dot{q}^e_3(\dot{q}^e_1 + \dot{q}^e_2)$$
$$- \frac{(\sin q^e_3)}{2}(\dot{q}^e_3)^2$$

$$\Phi(2, 13) = \Phi(2, 15) = g \sin q^e_{12}, \quad \Phi(2, 16) = g \sin q^e_{123}$$

$$\Phi(3, 1) = \Phi(3, 2) = \Phi(3, 3) = \Phi(3, 4) = \Phi(3, 5)$$
$$= \Phi(3, 6) = \Phi(3, 8) = \Phi(3, 11) = \Phi(3, 12)$$
$$= \Phi(3, 13) = \Phi(3, 14) = \Phi(3, 15) = 0$$

$$\Phi(3, 7) = \ddot{q}^e_3, \quad \Phi(3, 9) = \frac{(\sin q^e_{23})}{2}(\dot{q}^e_1)^2,$$

$$\Phi(3, 10) = \sin q^e_3\left(\frac{\dot{q}^e_1}{2} + \dot{q}^e_3\right)\dot{q}^e_1 + \frac{\sin q^e_3}{2}(2\dot{q}^e_1 + \dot{q}^e_2)\dot{q}^e_2$$

$$\Phi(3, 16) = g \sin q^e_{123}$$

$$\Omega_1 = \frac{m_1^e l_1^{e2}}{3}, \quad \Omega_2 = \frac{5m_2^e l_1^{e2}}{4}, \quad \Omega_3 = m_2^e l_1^e l_2^e,$$

$$\Omega_4 = \frac{m_2^e l_2^{e2}}{12}, \quad \Omega_5 = m_3^e l_1^{e2}, \quad \Omega_6 = m_3^e l_2^{e2},$$

$$\Omega_7 = \frac{m_3^e l_3^{e2}}{3}, \quad \Omega_8 = m_3^e l_1^e l_2^e, \quad \Omega_9 = m_3^e l_1^e l_3^e,$$

$$\Omega_{10} = m_3^e l_2^e l_3^e, \quad \Omega_{11} = \frac{m_2^e l_1^e}{2e}, \quad \Omega_{12} = m_2^e l_1^e,$$

$$\Omega_{13} = \frac{m_2^e l_2^e}{2}, \quad \Omega_{14} = m_3^e l_1^e, \quad \Omega_{15} = m_3^e l_2^e,$$

$$\Omega_{16} = \frac{m_3^e l_3^e}{2}$$

where $q_{jj}^e = q^e + q^e$ and $q_{jjj}^e = q^e + q^e + q^e$, $\quad \forall j = 1, 2, 3$; m_i^e, $\quad \forall i = 1, 2, 3$ denotes the thigh, calf, and ankle-foot mass of the exoskeleton system; g represents the acceleration due to gravity.